
Article:
Pascual-Gonzalez, C., Schileo, G., Khesro, A. et al. (4 more authors) (2017) Band gap evolution and a piezoelectric-to-electrostrictive crossover in (1 − x)KNbO3–x(Ba0.5Bi0.5)(Nb0.5Zn0.5)O3 ceramics. Journal of Materials Chemistry C, 5 (8). pp. 1990-1996. ISSN 2050-7534

https://doi.org/10.1039/c6tc05515j

Journal Name

ARTICLE

Band gap evolution and piezoelectric-to-electrostrictive crossover in (1-x)$KNbO_3$-x($Ba_{0.5}Bi_{0.5}$)($Nb_{0.5}Zn_{0.5}$)O_3 ceramics

Received 00th January 20xx,
Accepted 00th January 20xx

DOI: 10.1039/x0xx00000x

www.rsc.org/

Cristina Pascual-Gonzalez[a], Giorgio Schileo[b], Amir Khesro[b], Iasmi Sterianou[a], Dawei Wang[b], Ian M. Reaney[b], Antonio Feteira[a]

The band gap of (1-x)$KNbO_3$-x($Ba_{0.5}Bi_{0.5}$)($Nb_{0.5}Zn_{0.5}$)O_3 ($0 \leq x \leq 0.25$) ceramics narrows slightly from 3.22 eV for x=0 to 2.89 eV for x=0.25, in broad agreement with first-principle calculations [Phys. Rev. B 89, 235105 (2014)]. In addition, an unreported piezoelectric-to-electrostrictive crossover is observed in this compositional range, which is accompanied by a continuous decrease of the maximum electric field-induced strain due to the presence of a non-ferroelectric phase. An electrostriction coefficient of 0.023 m^4/C^2 is measured for x=0.05, whilst no electromechanical response is observed for non-ferroelectric x=0.25, even under an applied electric field of 80 kV/cm.

Introduction

Coupling of light absorption in ferroelectrics with properties such as photovoltage, photostriction and photocatalysis has been envisaged as a route to create novel photoactive devices.[1-8] Spontaneous polarization in ferroelectrics offers an internal electric field to effectively separate photogenerated charge carriers, enabling them to reach the surface and not only interact and react with molecules in the surrounding media but also to create photo-induced currents.[9] Solar energy harvesting using ferroelectrics such as $KNbO_3$ (KN) was recently proposed as a potential route for sustainable, non-hazardous, and economically viable technologies to reduce our reliance in fossil fuel.[10]

KN is a prototypical ferroelectric (FE) perovskite. In the classic work by Shirane et al[11], the room-temperature spontaneous polarisation of single-domain KN was reported as 41 ± 2 μC/cm^2. This large spontaneous polarisation was rationalised on the basis of the non-centrosymmetric position of Nb^{5+} cations within the NbO_6 octahedra. This distortion is driven by the hybridisation of the empty d-orbitals of Nb^{5+} with the O^{2-} p-orbitals. On cooling from high temperature, KN undergoes a series of structural phase transitions. A paraelectric-to-ferroelectric phase transition occurs at 410 °C, when the crystal symmetry of KN changes from cubic centrosymmetric ($Pm\bar{3}m$) to tetragonal non-centrosymmetric ($P4mm$). Two ferroelectric-to-ferroelectric phase transitions occur on further cooling. At 220 °C the crystal symmetry changes from tetragonal ($P4mm$) to orthorhombic ($Amm2$) and at −55 °C from orthorhombic ($Amm2$) to rhombohedral ($R3m$). These phase transitions are accompanied by anomalies in the temperature dependence of the relative permittivity, ε_r, of KN. Single-crystal KN exhibits a maximum ε_r of ~ 4000 at the Curie temperature of 410 °C, whereas at room-temperature it is ~1000. In ceramics, the room-temperature ε_r was been report to vary between ~300 and 800.[12-15] This wide range on ε_r values is linked to several aspects of the final microstructures, such as variations on density, texture and grain sizes. Fabrication of KN ceramics is difficult with problems mainly associated with unsuccessful densification, due to its low melting temperature (< 1100°C). In addition, the structural stability of KN ceramics encompassing residual $K_4Nb_6O_{17}$ is dramatically affected by moisture. To minimise the detrimental effects of moisture, several authors studied the impact of processing conditions[13, 16, 17] on KN and prescribed remedial procedures[14, 15]. For example, Matsumoto et al[18] demonstrated that through careful processing, including an addition of 1.2 wt% of $MnCO_3$ to reduce electrical conductivity and enhance densification, it is possible to prepared KN ceramics by the conventional solid state reaction route that show a respectable 0.22% electric-field induced strain under an unipolar field of 80 kV/cm. More recently, Lv et al[19] demonstrated the addition of ZnO to KN to improve to simultaneously improve the electrical properties and the resistance to moisture.

Interest in KN has been renewed by a recent proposal on its potential as a base material for both nanogenerators[20-22] and photovoltaic applications.[10, 23, 24] Grinberg et al[10] reported the preparation of (1-x)$KNbO_3$-x$BaNi_{0.5}Nb_{0.5}O_{3-\delta}$ (KBNNO) ceramics

[a] Christian Doppler Lab on Advanced Ferroic Oxides, Materials and Engineering Research Institute, Sheffield Hallam University, Howard Street, S1 1WB, Sheffield, United Kingdom
[b] Department of Materials Engineering and Science, The University of Sheffield, S1 4JD, Sheffield, United Kingdom
*Email - a.feteira@shu.ac.uk

Electronic Supplementary Information (ESI) available: XRD, Raman, water immersion test and Tauc plots data for stoichiometric $KNbO_3$ and K-deficient $K_{0.95}NbO_3$ ceramics See DOI: 10.1039/x0xx00000x

which exhibit high polarization (40 μC/cm^2) and band gaps as low as 1.1 eV. The combination of a low band gap with high polarization is achieved through ferroelectrically active Nb^{5+} combined with Ni^{2+} and O vacancies. However, this new ferroelectric oxide relies on the presence of a large concentration of oxygen vacancies, detrimental to polarization switching and which can also trap photogenerated carriers and increase the charge recombination rate. According to first-principles calculations, KN doped with Zn^{2+} for Nb^{5+}, charge compensated at the *A* sites with different combinations of higher valence cations, is a semiconducting ferroelectric with high spontaneous polarization. First principle calculations for $0.75KNbO_3$-$0.25(Ba_{0.5}Bi_{0.5})(Nb_{0.5}Zn_{0.5})O_3$ gave a value of ~37 μC/cm^2, which is typical for a robust ferroelectric material.[25] Moreover, it was also calculated that the band gap drops from 3.15 eV for orthorhombic $KNbO_3$ to 2.90 eV for $0.75KNbO_3$-$0.25(Ba_{0.5}Bi_{0.5})(Nb_{0.5}Zn_{0.5})O_3$. It was argued that Zn^{2+} substitution for higher-valence Nb^{5+} in $KNbO_3$ gives rise to increased repulsion between the O 2p and Zn 3d states and thereby to a higher valence band maximum (VBM). The shift up of the VBM is driven by the repulsion between the non-bonding $3d^{10}$ orbitals of Zn^{2+} and the $2p^6$ orbitals of O^{2-}. In addition, the conduction band minimum (CBM) which consists mainly of the Nb 4d states is essentially preserved from the parent $KNbO_3$. Hence, CBM is dependent on the off-centering direction of the B-site cation.

In this work, a comprehensive characterisation of the $(1-x)KNbO_3$-$x(Ba_{0.5}Bi_{0.5})(Nb_{0.5}Zn_{0.5})O_3$ (KN-BBNZ) system was carried out. Experimental results validate previous first principle calculations of the band gap for x=0.25, which also appeared to be non-ferroelectric. In addition, a piezoelectric-to-electrostrictive crossover, which is indicative of a ferroelectric-to-relaxor crossover was also unveiled. The normal-to-relaxor ferrorelectric crossover in Pb-free ceramics is now well documented and it has been recently reviewed by Shvartsman and Lupascu[26]. Interestingly, heterovalent substitution in $K_{0.5}Na_{0.5}NbO_3$ (KNN), which is isostructural with KN, induces quenched random fields due to the local charge imbalance and the local elastic fields. These fields hinder long-range ordering and leading to polar nanometric-size regions, often refer as PNRs. The degree of transformation into relaxor behavior varies between different systems, as observed for KNN-$SrTiO_3$[27] and KNN-$BiScO_3$[28] In the present system KN-BBZN, the frequency dependence of the dielectric properties decreases as the BBZN content decreases.

Finally, the evolution of the optical band gap and of the dielectric behaviour was discussed on the basis of the average and local crystal chemistries.

Experimental

$(1-x)KNbO_3$-$x(Ba_{0.5}Bi_{0.5})(Nb_{0.5}Zn_{0.5})O_3$ (KN-BBNZ) ceramics were prepared by the conventional mixed oxide route. The starting materials were high-purity grade K_2CO_3, Bi_2O_3, $BaCO_3$, Nb_2O_5, and ZnO powders (≥99%, ≥99.9%, 98%, 99.9% and ≥99% purity, respectively, Sigma-Aldrich). In order to evaluate the impact of eventual K loss due to volatilisation during high temperature processing[29], $KNbO_3$ and $K_{0.95}NbO_3$ (control sample, to mimic a substantial K loss due to volatilisation) ceramics were prepared and characterised. Those results are provided in the electronic supplementary information (ESI, Fig. S1 to S5).

The starting chemicals were weighed in the required molar ratios and intimately mixed in propanol using a ball mill and zirconia media. The dried slurries were subsequently calcined twice in air at 850 °C. Their purity and crystallinity were determined by x-ray diffraction (XRD) using a high-resolution diffractometer (CoK_α, 1.7989 Å, D8 Empyrean XRD, PANalytical™, Almelo, The Netherlands) operated at 40 kV and 40 mA, in the 2Θ range between 20 and 80, with 2Θ increments of 0.013 and counting time of ~600 s per step.

The calcined powders were finely milled and uniaxially pressed into pellets under an applied pressure of ~150 MPa. These green compacts were fired in air for 4 hours at temperatures ranging from 1070 to 1100 °C, using a controlled heating rate of 5 °C /min. The fired densities reached 96% of the theoretical density calculated from the XRD data. Ceramic microstructures (ESI, S6) were examined using a scanning electron microscope (model: Nova Nano 200, FEI, Brno, Czech Republic) equipped with a field emission gun. The samples were carbon coated before SEM in order to avoid charging. Depolarised Raman spectra were recorded in backscattering geometry with a spectrometer (InVia, Renishaw, New Mills, UK) equipped with a microscope objective of 50x magnification and using the 520 nm laser. Capacitance measurements in the frequency range 10 kHz to 1 MHz were carried out in unpoled ceramics using an LCR meter coupled with a tube furnace applying a heating/cooling rate of 1 C°/min.

The electromechanical response was recorded at room temperature using a ferroelectric tester (AixACCT TF 2000) by applying a high voltage triangular signal and measuring the strain using a laser interferometer. Diffuse reflectance ultraviolet and visible DRUV-vis spectra for KBBNZ ceramics were acquired at room temperature in the range 200-1600 nm using an UV-VIS-NIR Spectrophotometer (Shimadzu UV-3600). Fine $BaSO_4$ powder was used as a non-absorbing standard. To calculate band gaps, the following procedure was carried out. First, the Kubelka-Munk (K-M) function given below was calculated.

$$F(R) = \frac{(1-R)^2}{R}$$

where *R* is the experimental reflectance referred to the $BaSO_4$ standard. Hereafter, the K-M function (or *F(R)* curves) is considered to be proportional to the optical absorption. Hence, the absorption coefficient, α, can substituted by *F(R)* in the Tauc equation:

$$(h\nu\alpha)^{1/n} = A(h\nu - E_g) = [h\nu F(R)]^{1/n}$$

where h is the Planck's constant, ν is frequency of vibration, α is absorption coefficient, E_g is band gap and A is proportional constant. The value of the exponent n denotes the nature of the sample transition. For direct, the allowed transition is n=1/2, whilst for indirect, the allowed transition is n=2. Often it is difficult to

determine from a Tauc plot if a band gap is direct or indirect. Wang et al[25] postulated that the band gap of KN-BBZN x=0.25 is indirect, therefore, in this contribution, all Tauc representations for KN-BBNZ were carried out using n=2. Urbach energies, E_U, were calculated using the function:

$$\ln \alpha = \frac{h\nu}{E_U} = \ln F(R)$$

Results and Discussion

Crystal Structure

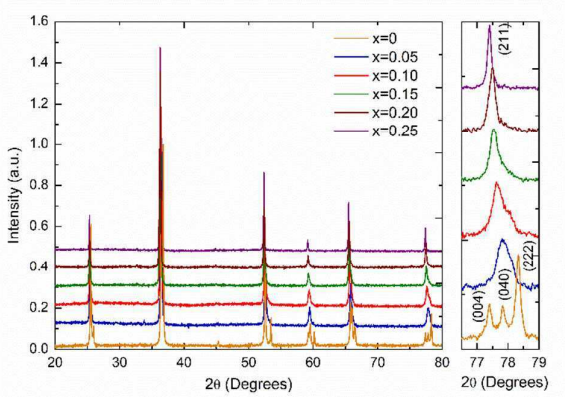

Figure 1. Room-temperature XRD data for (1-x)$KNbO_3$-x$(Ba_{0.5}Bi_{0.5})(Nb_{0.5}Zn_{0.5})O_3$ ceramics. (x increases from bottom to top).

Room-temperature X-ray diffraction (XRD) data for KN-BBNZ (0≤ x≤ 0.25) ceramics are shown in Fig. 1. All reflections for doped compositions shift continuously towards lower 2Θ angles, indicating an increase of the unit cell size with increasing x. This supports the co-solubility of Ba, Bi and Zn into the KN lattice according to the $K_{1-x}Ba_{x/2}Bi_{x/2}Nb_{1-x/2}Zn_{x/2}O_3$ formula. The XRD pattern of KN (x=0) ceramics exhibits well-defined sharp peaks which can be indexed to an orthorhombic cell with *Amm2* symmetry. Lattice parameters for KN ceramics were calculated as a=3.9708(1) Å, b=5.6932(1) Å and c=5.7129(1) Å, which are in broad agreement with the ICDD card No. 00-032-0822. The inset of Fig.1 shows the presence of a triplet for x=0 associated with [27, 30], {400} and {222}, but within the resolution of our measurements only a single peak is visible for the other compositions.

For x=0.05, a shoulder is visible on the higher 2θ side indicating a distortion away from cubic symmetry. This composition still shows an *average* orthorhombic crystal symmetry. For x=0.10 and 0.15, XRD data are consistent with the coexistence of an orthorhombic KN-based phase (space group *Amm2*) and cubic phase (space group $Pm\bar{3}m$). The relative content of orthorhombic phase falls from ~70% for x=0.10 to ~ 30% for x=0.15. In both ceramics, the existence of the ferroelectric orthorhombic KN-based phase, is also corroborated by the appearance of two dielectric anomalies as a function of temperature, as discussed later. The anomalies are associated with the orthorhombic-to-tetragonal and the tetragonal-to-cubic structural phase transitions. For x=0.20 and 0.25, the diffraction data are consistent with an *average* cubic crystal symmetry however, Raman spectra presented in Fig. 3 demonstrate that actually none of these compositions show a *local* structure that is truly cubic. Average lattice metrics calculated from Rietveld refinement of XRD data for all KN-BBNZ ceramics are given in Table I of the *electronic supplementary information* (ESI, Table I). The unit cell volume for the orthorhombic phase ($Amm2$) increases linearly up to x=0.10, at this concentration orthorhombic and cubic symmetries coexist, but beyond this concentration the unit cell volume for the cubic phase also increases linearly, as shown in Fig. 2. The variation of the cell volume for the single-phase compositions follows Vegard's law.

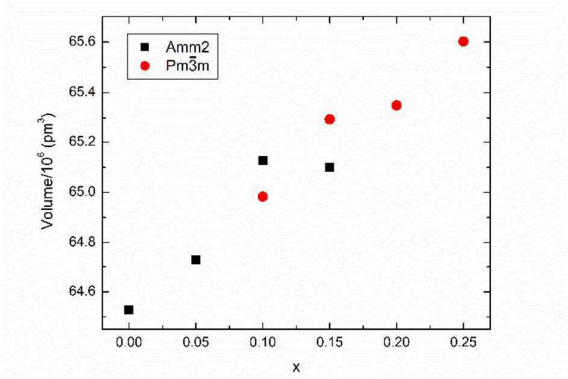

Figure 2. Compositional variation of the unit cell volume for (1-x)$KNbO_3$-x$(Ba_{0.5}Bi_{0.5})(Nb_{0.5}Zn_{0.5})O_3$ (0≤x≤0.25) ceramics.

Raman Spectroscopy

Room-temperature Raman spectra for KN-BBNZ (0≤ x≤ 0.25) ceramics are presented in Fig. 3. From group theory analysis, orthorhombic KN (x=0) exhibits 12 Raman active optical modes of $4A_1 + 4B_1 + 3B_2 + A_2$ symmetries, which can be separated into translational modes of isolated K^+ and internal modes of the NbO_6 octahedra.

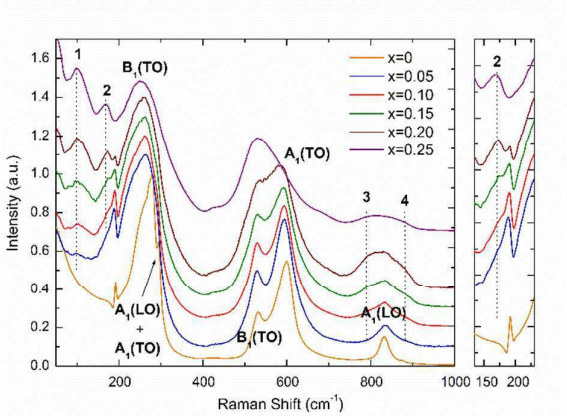

Figure 3. Room-temperature Raman spectra for (1-x)$KNbO_3$-x$(Ba_{0.5}Bi_{0.5})(Nb_{0.5}Zn_{0.5})O_3$ (0≤x≤0.25) ceramics. (x increases from bottom to top)

Modes in the KN Raman spectrum are labelled according to the single-crystal assignment by Quittet et al[31]: (i) a mixed sharp mode at 192 cm^{-1}; (ii) a Fano-type interference dip at 197 cm^{-1}; (iii) a broad B_1 (TO) mode centered at 250 cm^{-1}; (iv) a B_1 (TO) at 272 cm^{-1}; (v) a sharp mode at 278 cm^{-1}; (vi) another mode at 294 cm^{-1}; (vii) a B_1(TO) mode at ~ 532 cm^{-1}; (viii) a A_1(TO) mode at ~ 600 cm^{-1} and (ix) a low intensity A_1(LO) mode at 831 cm^{-1}. The sharp mode at 192 cm^{-1} is a mixed B_1(TO), A_1(TO), A_1(LO) and B_2(TO) mode. Similarly, the mode at 278 cm^{-1} is due to a broad A_1(TO) combined with a sharp A_2, whilst the sharp mode at 294 cm^{-1} is due to A_1(LO) and A_1(TO). However because of the resolution limit of the instrument they appear merged as a single peak. Upon doping new modes emerged, which here are labelled as 1, 2, 3 and 4, because at this stage information on their origin is purely speculative. Mode 1 emerges around ~100 cm^{-1}, whereas mode 2 appears at ~175 cm^{-1}, as a shoulder to the sharp mixed mode at 192 cm^{-1}. These modes are fairly static, as they only shift by ~ 1 cm^{-1} over the entire compositional range, but their relative intensity increases continuously. In the past, they have been associated to A-O vibrations within nm-sized clusters rich in either Bi^{3+} and/or K^+ cations. Modes 3 and 4 appear on both sides of the high frequency A_1(LO) mode. These have been previously associated with breathing of the BO_6 octahedra, when occupied by different B-cations. Doping also leads to softening of some modes. For example, the A_1(TO) mode at ~ 600 cm^{-1} for x=0 gradually softens to 585 cm^{-1} for x=0.20, due to the increase in the unit cell volume, as shown in Fig. 2. Indeed, softening of this O-Nb-O symmetric stretching mode is known to occur in undoped KN with increasing temperature, as expected from the lattice thermal expansion, which implies a lowering of the force constants. In contrast, the B_1(TO) mode at ~ 532 cm^{-1} shows no compositional shift. The relative intensity of the A_1(TO) in relation to the B_1(TO) decreases continuously with increasing x. For x=0.25, the A_1(TO) mode is considerably less intense than the B_1(TO).

The occurrence of long-range polarisation in KN is ultimately associated with the presence of the (i), (ii) and (vi) modes, which therefore can be used to monitor the polar nature of KN-based solid solutions, as shown by Luisman et al[32]. Hence, the presence of the (i), (ii) and (vi) modes in the spectra of KN-BBNZ ceramics support the occurrence of spontaneous polarisation in ceramics with x≤0.20. Later, it will be shown through polarisation vs electric field (P-E) measurements that this polarisation is reversible. Hence, the presence of spontaneous polarisation even in x=0.20 suggests the presence of some residual orthorhombic ($Amm2$) phase, but at a level below the detection limit of the in house XRD. This is consistent with the decrease of the relative intensity of mode (ii) in comparison with mode 2, as illustrated in the expanded region of Fig. 3. The presence of this residual orthorhombic phase is also responsible for dielectric anomalies in x=0.20 ceramics, as shown later. Finally, the absence of (i), (ii) and (vi) modes from the x=0.25 spectrum, suggests a complete lack of long-range polarisation, which complete rules out the occurrence of ferroelectricity in $0.75KNbO_3$-$0.25(Ba_{0.5}Bi_{0.5})(Nb_{0.5}Zn_{0.5})O_3$. Again, the absence of ferroelectricity will be latter corroborated through P-E measurements in combination with strain vs electric (S-E) curves and dielectric data. Indeed, the absence of a measurable electromechanical response under an electric field as large as 80 kV/cm; combined with a dielectric response free of anomalies is consistent with ceramics exhibiting an *average* cubic crystal symmetry, as determined from the XRD traces shown in Fig. 1.

Nevertheless, the presence of intense broad modes in the Raman spectrum of x =0.25 ceramics, Fig. 3, provides ample evidence that their *local* crystal symmetry cannot be described by the cubic $Pm\bar{3}m$ space group. The presence of K^+, Ba^{2+} and Bi^{+3} in the A-sites and Nb^{+5} and Zn^{2+} in the B-sites not only induce local strains due to the difference in ionic radii, but also due to the hybridization between the $6s^2$ lone-pair of electrons of Bi^{3+} with both empty $6p^0$ orbitals of Bi^{3+} and $2p^6$ electrons of O^{2-} which foreshortens the Bi-O covalent bonds. Bi^{3+} cations in perovskite compounds tend to off-center, often inducing rhombohedral distortions, thereby relieving the tensile bond strain of shorter Bi-O bonds. All the aforementioned *local* deformations allow for strong Raman scattering on materials, whose *average* crystal structure may be described by the cubic $Pm\bar{3}m$ space group, since the ions are locally displaced away from the centre of inversion. Octahedral tilting due to smaller Bi^{3+}, which is a common distortion mechanism for reducing the A-O bond strain in perovskites, can be partially counteracted by the equivalent concentration of larger Ba^{2+} in KN-BBNZ ceramics. In summary, the Raman spectrum for x=0.25 provides a strong spectroscopic indication for the occurrence of short-range lattice deformations, which could not be resolved from the XRD data, but also rules out spontaneous polarisation in those ceramics. In addition, *In-situ* Raman analysis between -180 and 280°C suggested the crystal symmetry for x=0.25 is unchanged in this temperature range, in contrast with $KNbO_3$, as shown in Fig. S7 in the ESI. Finally, the increasing broadening of modes in the Raman spectra with increasing x, is consistent with increasing lattice disorder, which may be behind the dielectric response and the emergence of Urbach tails in optical response, as discussed later.

Dielectric and Electromechanical Properties

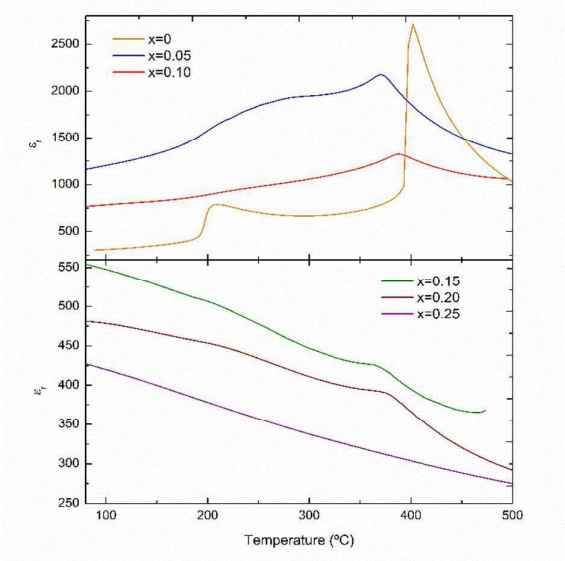

Figure 4. Temperature dependence of ε_r for $(1-x)KNbO_3$-$x(Ba_{0.5}Bi_{0.5})(Nb_{0.5}Zn_{0.5})O_3$ ($0 \leq x \leq 0.25$) ceramics.

The temperature dependence of the permittivity, ε_r for KN-BBNZ ceramics (x=0, 0.05, 0.15 and 0.25) measured at 100 kHz is illustrated in Fig. 4. This gives a general overview on the impact of doping in the phase transitions. Interestingly, all doped compositions exhibit a larger ε_r at lower temperatures than pure KN, but which decreases with increasing x.

KN (x=0) shows two maxima at ~ 205 °C and ~ 400 °C, respectively. Those two dielectric anomalies are associated to the orthorhombic-to-tetragonal and the tetragonal-to-cubic structural phase transitions, respectively. The highest temperature maximum corresponds to the Curie temperature, T_c. With increasing x, T_c initially drops ~370 °C for x=0.05, then it increases to ~387 °C for x=0.10, subsequently dropping to ~370 °C for x=0.15. This non-monotonic T_c variation occurs within the multiphase composition range, which suggests a non-homogeneous distribution of dopants between the orthorhombic and cubic phases. As aforementioned, x=0.20 still shows dielectric anomalies, due to a residual orthorhombic phase, which was not detected in XRD traces because it is present at levels below the detection limit of the technique. Finally, for x=0.25, ε_r decreases continuously with increasing temperature. No dielectric anomalies are detected in this temperature range, as expected from the XRD data, Fig. 1, which suggests that this composition has an *average* crystal structure. Nevertheless, it is worth noting that the ε_r is considerably large for a truly cubic structure, in agreement with the Raman analysis, which point out the occurrence of local distortions. Frequency dependent measurements of the relative permittivity and dielectric loss is provided for individual compositions in ESI, Fig. S8. . KN (x=0) shows a room-temperature ε_r of ~300, as shown in Fig. S8a. A strong frequency dependence of both ε_r and tan θ is observed for x=0.05 and 0.10, as illustrated in Fig. S8b and S8c, respectively. The temperature for the ε_r anomalies remains almost unaltered, but it magnitude decreases with increasing frequency. Since, tan θ also decreases with increasing frequency, this frequency dependency is different from that observed for conventional relaxors such as $Pb(Mg_{1/3}Nb_{2/3})O_3$. Nevertheless, it is consistent with results observed for some KNN-based solid solutions.[27] For x≥0.15 the frequency dependence is much less pronounced, as shown in Fig. S8d and S8e.

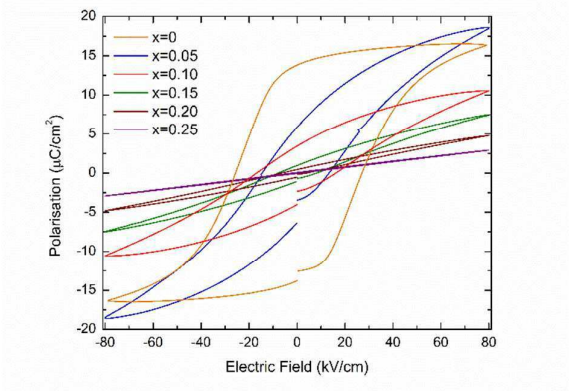

Figure 5. P-E measurements from (1-x)$KNbO_3$-x$(Ba_{0.5}Bi_{0.5})(Nb_{0.5}Zn_{0.5})O_3$ (0≤x≤0.25) ceramics.

Polarisation vs electric field (P-E) and strain vs electric field (S-E) loops measured at room temperature for KBBNZ ceramics under an electric field of 80 kV/cm, are shown in Fig. 5. Undoped KN (x = 0) exhibits a P–E loop typical of a ferroelectric response, as shown in Fig. 5.

KN ceramics show a maximum polarisation, P_{max}, of ~16.4 μC/cm^2, a remnant polarization, P_r, of ~13.8 μC/cm^2 and a coercive field, E_c, of ~26 kV/cm. When $(Ba_{0.5}Bi_{0.5})(Nb_{0.5}Zn_{0.5})O_3$ is substituted into the KN lattice, both P_r and E_c decrease dramatically and the P-E loops become increasingly slimmer as shown in Fig. 5, whereas the S-E curves evolve from a butterfly shape (which is typical for FE response, due to domain switching) to a parabolic shape (as expected for an electrostrictive response), as shown in Fig. 6.

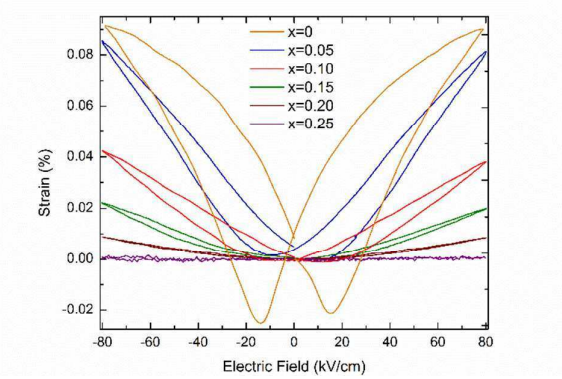

Figure 6. S-E measurements for (1-x)$KNbO_3$-x$(Ba_{0.5}Bi_{0.5})(Nb_{0.5}Zn_{0.5})O_3$ (0≤x≤0.25) ceramics.

The bipolar electric-field induced strain for KN (x=0) reaches about 0.091% under a field of 80 kV/cm, as shown in Fig. 6. The strain curve shows that the negative strain can reach ~0.02%, which is due to ferroelectric domain and domain wall switching. For x=0.05, P_r is ~ 6 μC/cm^2, which is roughly 2.5 times smaller than for KN, the maximum achievable strain under an electric field of 80 kV/cm is ~ 0.082%. For the multiphasic (orthorhombic + cubic) x=0.10, 0.15 and 0.20, the S-E responses show almost parabolic shapes, as shown in Fig. 6, and their maximum achievable strains drop to ~ 0.041%, 0.021% and 0.009%, respectively (ESI, Fig. S9). This electrostrictive-like response can be modelled according to the $S=QP^2$ relationship, where S, Q and P represent the strain, electrostriction coefficient and polarisation, respectively. For example for x=0.05, Q was calculated to be 0.023 m^{4}C^{-2} (ESI, Fig. S10). This value is even larger than that of the well-known electrostrictive material $Pb(Mg_{1/3}Nb_{2/3})O_3$-$PbTiO_3$ (PMN-7PT) which have Q of 0.017 m^{4}C^{-2} with a maximum strain of 0.12 % at 40 kV/cm. However the value of strain of x=0.05 is comparatively low. Electrostriction in Pb-free materials has been investigated in recent years.[33-36] Q values ranging from 0.021 to 0.027 m^4/C^2 were reported in antiferroelectric $Bi_{0.5}Na_{0.5}TiO_3$–$BaTiO_3$–$K_{0.5}N_{0.5}NbO_3$ ceramics[37]. More recently, Pb-free ferroelectric ceramics were reported to exhibit giant electrostrictive coefficients as large as 0.05

m^4C^{-2}.[38] Temperature dependence of the electric-field induced strain for x=0.05 is moderate (~13%), as illustrated by the unipolar measurements in ESI, Fig. S11. Finally, for single-phase x=0.25 with an *average* cubic structure, the P-E curve is virtually linear (hysteresis free) and a maximum polarisation of ~ 2.9 μC/cm^2 is measured at 80 kV/cm, as shown in Fig. 5. This composition does not show any measurable field-induced strain, as shown in Fig. 6. At this stage is still unclear why x=0.05 shows a higher field induced maximum polarisation than KN, but a lower field-induced strain. Many reasons such as grain size and orientation, domain size and density, etc can be speculated to be at the origin of this counterintuitive result.

Hence, the piezoelectric response for KN (x=0) arises from the macroscopic absence of a center of symmetry, and the butterfly-shaped S-E curves are due to domain switching, whereas for x=0.05 the banana-shaped response is associated with nanoregions with fluctuating polarisation (which may be associated with the Raman modes 1 and 2, in Fig. 3). Indeed, the lone-pair of electrons brought by Bi^{3+} may play an important role in this nanodomain process, possibly through the adjustment of the orientation of the lone-pair and the associated dipole moment with the applied electric field. The polar nanoregions respond to the applied electric field and may grow up to microscale.

The piezoelectric-to-electrostrictive crossover in the $KNbO_3$-$(Ba_{0.5}Bi_{0.5})(Nb_{0.5}Zn_{0.5})O_3$ system can be interpreted by competition induced by a mixture of covalent and ionic bonds and a distribution of effective cation radii which occurs due to the presence of K^+, Bi^{3+} and Ba^{2+} in the A- and Nb^{5+} and Zn^{2+} B-sites of the perovskite structure. The incorporation of Zn^{+2} in the B-site disrupts the Nb-O bonding, which is responsible for the long-range ordered displacement of Nb^{+5}. This gives rise to a distribution of bond lengths, and this lattice disturbance affects the balance between long-range dipolar Coulombic forces and short-range repulsion forces, which determines the occurrence of ferroelectricity in the perovskite structure. Disruption of this balance is ultimately responsible for the disappearance of the long-range polar ordering, as indicated by the absence of the 192 cm^{-1} sharp mode from the Raman spectrum of x=0.25. In the x= 0.10-0.20 range, the field induced strain decreases because of the increasing volume fraction of the cubic phase which, contrary to previous first principle calculations, was proved to be non-ferroelectric.

Optical band gaps

The excitation across the band gap in KN-BBNZ ceramics is essentially a charge transfer from the O 2p states at the valence band maximum (VBM) to the transition-metal d states at the conduction band minimum (CBM). Some insight into the band structure and other charge transitions can be gathered from the response to photons of different energies. Here, diffuse reflectance spectroscopy was carried out using photons with wavelengths ranging from 200 to 1600 nm. The band gaps for KN-BBNZ ceramics were determined using the Tauc plots in Fig. 7 and are listed in Table II in the ESI.

The band gap energies were obtained from the intercept of the tangent line in the plot of $[h\nu F(R)]^{1/2}$ vs energy. The indirect band gap of (1−x)$KNbO_3$-x$(Ba_{0.5}Bi_{0.5})(Nb_{0.5}Zn_{0.5})O_3$ (0≤x≤0.25) ceramics varies from 3.22 eV for x=0 to 2.89 eV for x=0.25, in broad agreement with first-principle calculations[25], but also with experimental results for $KNbO_3$.[4, 39] Moreover, these band gaps are consistent with the ability of KN-BBNZ ceramics to withstand electric fields as high as 80 kV/cm, as previously shown in Fig. 5 and 6.

Crystal chemistry arguments can be recalled to explain the moderated band gap narrowing as follows: (i) the replacement of Nb^{5+} by Zn^{2+} creates underbonded O^{2-} adjacent to the Zn^{2+}, which form ZnO_6 octahedra, (ii) Bi^{3+} which tend to be off-center, creating short, strong Bi-O (covalent) bonds that partially compensate for the aforementioned loss of B-O bonding (iii) Ba^{2+} do not off-center and are less prone to compensate the decrease of B-O bonding. As a result, the repulsion between the non-bonding O charge densities and Zn 3d states is relatively weak, leading to a moderate upshift of valence band maxima (VBM), which is composed of O 2p and Zn 3d states.[25]

It is worth noting that the observed Raman shift of the broad A_1 (TO_1), Fig. 3, may be a manifestation of the strong Bi-O bonds, whereas the general broadening of the Raman modes results from increased lattice disorder, which manifests itself by the emergence of Urbach tails, as indicated by the arrow in Fig. 7. From analysis of the Urbach tails, it is possible to obtain information pertaining to the dynamics of the electronic transitions, and in principle to evaluate the impact of defects on those transitions. For example, the Urbach energy, E_u, for KN-BBNZ x=0.25 was calculated as 0.22 eV.

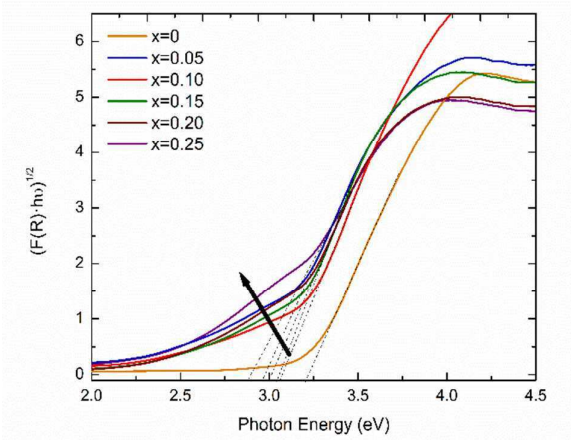

Figure 7. Tauc plot for indirect band gaps for (1-x)$KNbO_3$-x$(Ba_{0.5}Bi_{0.5})(Nb_{0.5}Zn_{0.5})O_3$ (0≤x≤0.25) ceramics.

In summary, a combination of competition between covalent and ionic bonds and a distribution of effective cation radii in the $KNbO_3$-$(Ba_{0.5}Bi_{0.5})(Nb_{0.5}Zn_{0.5})O_3$ system leads simultaneously to a piezoelectric-to-electrostrictive crossover and a modest narrowing of the optical band gaps.

Conclusions

The band gap evolution and the piezoelectric-to-electrostrictive crossover in the (1-x)$KNbO_3$-x($Ba_{0.5}Bi_{0.5}$)($Nb_{0.5}Zn_{0.5}$)O_3 ceramics arise from a distribution of bond lengths brought in by the larger Ba^{2+} and K^+ ions, which create oversized A-site cages for Bi^{3+}ions. This results in off-centering of Bi^{3+} in order to create shorter Bi-O bonds and thereby relieve the tensile bond strain. Zn^{2+} in B-sites leads also to substantial lattice disorder, resulting in a gradual disappearance of long-range reversal polarisation and a moderate narrowing of the optical band gap, by a moderate upshift of the VBM. The band gap of KN-BBNZ x=0.25 is 2.89 eV, which is in agreement with previous first principle calculations[25], however it is non-ferroelectric at room temperature.

Acknowledgements

Cristina Pascual-Gonzalez acknowledges the financial support of a VC scholarship from SHU. Ian M. Reaney acknowledges the support of the Engineering and Physical Sciences Research Council through EP/L017563/1.

References

1. F. Wang, I. Grinberg, L. Jiang, S. Young, P. Davies and A. Rappe, *Ferroelectrics*, 2015, **483**, 1-12.
2. T. Zhang, K. Zhao, J. Yu, J. Jin, Y. Qi, H. Li, X. Hou and G. Liu, *Nanoscale*, 2013, **5**, 8375-8383.
3. J. Lombardi, F. Pearsall, W. Li and S. O'Brien, *Journal of Materials Chemistry C*, 2016, **4**, 7989-7998.
4. P. Wu, G. Wang, R. Chen, Y. Guo, X. Ma and D. Jiang, *RSC Advances*, 2016, **6**, 82409-82416.
5. G. Wang, Y. Huang, A. Kuang, H. Yuan, Y. Li and H. Chen, *Inorganic Chemistry*, 2016, **55**, 9620-9631.
6. Y. Wang, X. Kong, W. Tian, D. Lei and X. Lei, *RSC Advances*, 2016, **6**, 58401-58408.
7. A. Bhatnagar, A. Chaudhuri, Y. Kim, D. Hesse and M. Alexe, *Nature Communications*, 2013, **4**.
8. Q. Fu, X. J. Wang, C. Y. Li, Y. Sui, Y. P. Han, Z. Lv, B. Song and P. Xu, *RSC Advances*, 2016, **6**, 108883-108887.
9. B. Modak and S. Ghosh, *Rsc Advances*, 2016, **6**, 9958-9966.
10. I. Grinberg, D. West, M. Torres, G. Gou, D. Stein, L. Wu, G. Chen, E. Gallo, A. Akbashev, P. Davies, J. Spanier and A. Rappe, *Nature*, 2013, **503**, 509-512.
11. G. Shirane, H. Danner, A. Pavlovic and R. Pepinsky, *Physical Review*, 1954, **93**, 672-673.
12. C. Pascual-Gonzalez, G. Schileo and A. Feteira, *Applied Physics Letters*, 2016, **109,** 9132902.
13. D. Kim, M. Joung, I. Seo, J. Hur, J. Kim, B. Kim, H. Lee and S. Nahm, *Journal of the European Ceramic Society*, 2014, **34**, 4193-4200.
14. H. Birol, D. Damjanovic and N. Setter, *Journal of the American Ceramic Society*, 2005, **88**, 1754-1759.
15. K. Kakimoto, I. Masuda and H. Ohsato, *Journal of the European Ceramic Society*, 2005, **25**, 2719-2722.
16. J. Kim, D. Kim, I. Seo, J. Hur, J. Lee, B. Kim and S. Nahm, *Sensors and Actuators A-Physical*, 2015, **234**, 9-16.
17. J. Acker, H. Kungl and M. Hoffmann, *Journal of the European Ceramic Society*, 2013, **33**, 2127-2139.
18. K. Matsumoto, Y. Hiruma, H. Nagata and T. Takenaka, *Ceramics International*, 2008, **34**, 787-791.
19. X. Lv, Z. Y. Li, J. G. Wu, D. Q. Xiao and J. G. Zhu, *Acs Applied Materials & Interfaces*, 2016, **8**, 30304-30311.
20. M. R. Joung, H. B. Xu, I. T. Seo, D. H. Kim, J. Hur, S. Nahm, C. Y. Kang, S. J. Yoon and H. M. Park, *Journal of Materials Chemistry A*, 2014, **2**, 18547-18553.
21. Y. Yang, J. Jung, B. Yun, F. Zhang, K. Pradel, W. Guo and Z. Wang, *Advanced Materials*, 2012, **24**, 5357-5362.
22. J. Jung, C. Chen, B. Yun, N. Lee, Y. Zhou, W. Jo, L. Chou and Z. Wang, *Nanotechnology*, 2012, **23**.
23. L. Yu, J. Jia, G. Yi, Y. Shan and M. Han, *Materials Letters*, 2016, **184**, 166-168.
24. F. Wang and A. Rappe, *Physical Review B*, 2015, **91**, 165124.
25. F. Wang, I. Grinberg and A. Rappe, *Physical Review B*, 2014, **89**, 235105.
26. V. V. Shvartsman and D. C. Lupascu, *Journal of the American Ceramic Society*, 2012, **95**, 1-26.
27. Y. P. Guo, K. Kakimoto and H. Ohsato, *Solid State Communications*, 2004, **129**, 279-284.
28. H. L. Du, W. C. Zhou, F. Luo, D. M. Zhu, S. B. Qu, Y. Li and Z. B. Pei, *Journal of Applied Physics*, 2008, **104**, 034104.
29. S. Priya and S. Nahm, *Lead-Free Piezoelectrics*, Springer New York, 2011.
30. J. Acker, H. Kungl, R. Schierholz, S. Wagner, R. Eichel and M. Hoffmann, *Journal of the European Ceramic Society*, 2014, **34**, 4213-4221.
31. A. Quittet, M. Bell, M. Krauzman and P. Raccah, *Physical Review B*, 1976, **14**, 5068-5072.
32. L. Luisman, A. Feteira and K. Reichmann, *Applied Physics Letters*, 2011, **99,** 192901.
33. W. Bai, L. Li, W. Wang, B. Shen and J. Zhai, *Solid State Communications*, 2015, **206**, 22-25.
34. F. Wang, C. Jin, Q. Yao and W. Shi, *Journal of Applied Physics*, 2013, **114**, 027004.
35. R. Z. Zuo, H. Qi, J. Fu, J. F. Li, M. Shi and Y. D. Xu, *Applied Physics Letters*, 2016, **108**, 142902.
36. S. T. Zhang, F. Yan, B. Yang and W. W. Cao, *Applied Physics Letters*, 2010, **97**, 142902.
37. S. T. Zhang, A. B. Kounga, W. Jo, C. Jamin, K. Seifert, T. Granzow, J. Rodel and D. Damjanovic, *Advanced Materials*, 2009, **21**, 4716-4720.
38. L. Jin, R. J. Huo, R. P. Guo, F. Li, D. W. Wang, Y. Tian, Q. Y. Hu, X. Y. Wei, Z. B. He, Y. Yan and G. Liu, *Acs Applied Materials & Interfaces*, 2016, **8**, 31109-31119.
39. H. Shi, C. Zhang, C. Zhou and G. Chen, *RSC Advances*, 2015, **5**, 93615-93622.

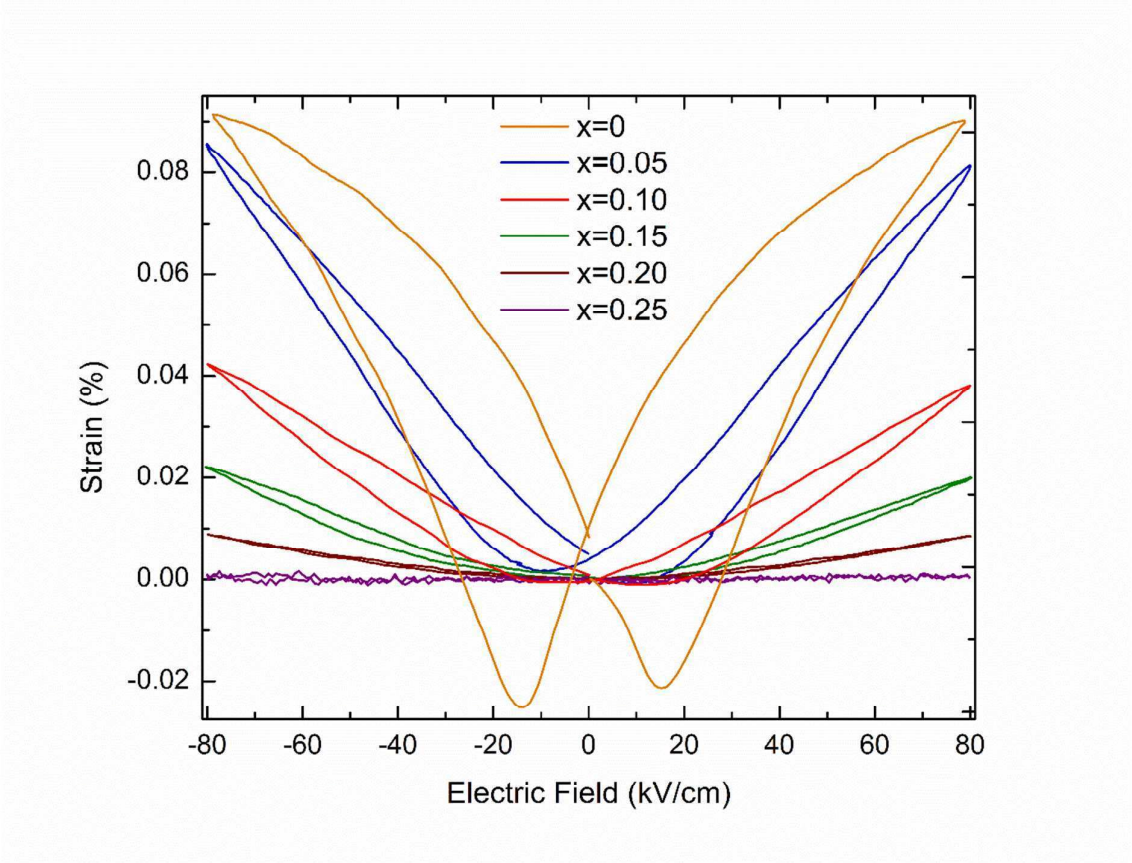

Piezoelectric-to-electrostrictive crossover in (1-x)$KNbO_3$-x($Ba_{0.5}Bi_{0.5}$)($Nb_{0.5}Zn_{0.5}$)O_3